Biophysical Journal
Article

Biophysical Society

Motor Dynamics Underlying Cargo Transport by Pairs of Kinesin-1 and Kinesin-3 Motors

Göker Arpağ,[1] Stephen R. Norris,[2,3] S. Iman Mousavi,[1] Virupakshi Soppina,[2] Kristen J. Verhey,[2,3] William O. Hancock,[4,*] and Erkan Tüzel[1,*]

[1]Department of Physics, Worcester Polytechnic Institute, Worcester, Massachusetts; [2]Department of Biophysics and [3]Department of Cell and Developmental Biology, University of Michigan, Ann Arbor, Michigan; and [4]Department of Biomedical Engineering, Pennsylvania State University, State College, Pennsylvania

ABSTRACT Intracellular cargo transport by kinesin family motor proteins is crucial for many cellular processes, particularly vesicle transport in axons and dendrites. In a number of cases, the transport of specific cargo is carried out by two classes of kinesins that move at different speeds and thus compete during transport. Despite advances in single-molecule characterization and modeling approaches, many questions remain regarding the effect of intermotor tension on motor attachment/reattachment rates during cooperative multimotor transport. To understand the motor dynamics underlying multimotor transport, we analyzed the complexes of kinesin-1 and kinesin-3 motors attached through protein scaffolds moving on immobilized microtubules in vitro. To interpret the observed behavior, simulations were carried out using a model that incorporated motor stepping, attachment/detachment rates, and intermotor force generation. In single-molecule experiments, isolated kinesin-3 motors moved twofold faster and had threefold higher landing rates than kinesin-1. When the positively charged loop 12 of kinesin-3 was swapped with that of kinesin-1, the landing rates reversed, indicating that this "K-loop" is a key determinant of the motor reattachment rate. In contrast, swapping loop 12 had negligible effects on motor velocities. Two-motor complexes containing one kinesin-1 and one kinesin-3 moved at different speeds depending on the identity of their loop 12, indicating the importance of the motor reattachment rate on the cotransport speed. Simulations of these loop-swapped motors using experimentally derived motor parameters were able to reproduce the experimental results and identify best fit parameters for the motor reattachment rates for this geometry. Simulation results also supported previous work, suggesting that kinesin-3 microtubule detachment is very sensitive to load. Overall, the simulations demonstrate that the transport behavior of cargo carried by pairs of kinesin-1 and -3 motors are determined by three properties that differ between these two families: the unloaded velocity, the load dependence of detachment, and the motor reattachment rate.

INTRODUCTION

Cargo transport by kinesin motor proteins is essential for cell survival and is particularly important in neurons, in which motors from the kinesin-1, -2, and -3 families transport a diverse range of cargo both in axons and dendrites (1,2). Most neuronal transport is bidirectional due to cargo having both kinesin and dynein motors bound (3–6), and the resulting transport involves a complex and poorly understood interplay between these antagonistic motors. Interestingly, there are many documented instances in which two classes of kinesins that have different speeds are simultaneously attached to a single cargo (reviewed in (7)). For instance, isolated neuronal vesicles were shown to contain both kinesin-1 and kinesin-2 motors along with dynein, and bidirectional transport of these cargo could be reconstituted in vitro (4). Cotransport of synaptophysin-containing vesicles by kinesin-1 and kinesin-3 motors in cultured neurons was also demonstrated, and knockout of the slower kinesin-1 led to increases in the cargo transport velocity, suggesting both motors are contributing to transport (3). Finally, intraflagellar transport in Caenorhabditis *elegans* sensory cilia results from cotransport by two different kinesin-2 motors having different unloaded velocities (8,9).

Uncovering the motor dynamics underlying multimotor transport is challenging because although cargo characteristics such as instantaneous velocity, run length, and directional

Submitted August 1, 2017, and accepted for publication January 3, 2019.

*Correspondence: wohbio@engr.psu.edu or etuzel@wpi.edu

Göker Arpağ's present address is Cell and Developmental Biology, Vanderbilt University, Nashville, Tennessee.

Virupakshi Soppina's present address is Department of Biological Engineering, Indian Institute of Technology Gandhinagar, Gandhinagar, Gujarat, India.

Editor: Stefan Diez.

https://doi.org/10.1016/j.bpj.2019.01.036

switching frequency can be precisely measured, the fraction of time each motor spends attached to the microtubule and the effect of intermotor tension on motor attachment/reattachment rates are difficult to track experimentally. Although a number of modeling approaches have been used to uncover the motor-motor dynamics underlying cargo transport (10–16), efforts are hampered by the lack of strong experimental constraints for load-dependent off rate and motor reattachment rate parameters that are key determinates of the overall transport properties. Kinesin-3 motors (KIF1A/Unc-104 as well as KIF1, KIF13, KIF14, KIF16, and KIF28 (17)) are distinctive in being fast transporters and having a positively charged loop 12 (K-loop) that electrostatically interacts with the negatively charged C-terminal tail of tubulin to enhance motor on rates (18). Experimental and modeling efforts suggest that although loop 12 enhances microtubule-motor association, the off rate of kinesin-3 is highly sensitive to load (11,19,20), implying that kinesin-3 on and off kinetics are fast during cotransport with either slower kinesins or with dynein.

The goal in this work is to uncover the intermotor coordination that occurs when a cargo is driven by one kinesin-1 and one kinesin-3 motor along a single microtubule. Previous work provided evidence of negative interference between pairs of kinesin-1 motors (21), and studies of cotransport by kinesin-1 and kinesin-3 have suggested that kinesin-1 activity dominates the transport behavior (3,11,20). One unknown parameter in all of these studies is the microtubule reattachment rate of cargo-bound motors that have dissociated from the microtubule, $k_{reattach}$. This reattachment rate determines whether transport primarily results from the action of one or multiple motors; if reattachment is slow relative to the rates motors detach from the microtubule, then single-motor transport will dominate, whereas if the opposite is true, then two-motor transport will dominate. In previous modeling work investigating the relative contributions of different motors in multimotor transport, $k_{reattach}$ has often been assumed to have a static value of 5 s^{-1} for all motors (22) or has been set to infinity in situations in which the presence of high densities of motors diminish the importance of this rate (11). Here, we use mutant kinesin-1 and kinesin-3 motors having different microtubule on rates to investigate the influence of this parameter on multimotor transport. We use a model for cargo transport by two kinesins based on our previous model for multimotor transport in the gliding assay (11), and we use cargo velocities to tune model parameters. Model simulations suggest that the motor reattachment rate is 1- to 10-fold faster than the motor off rate in this system, which is considerably slower than what is predicted from a first principles approach. By using a model to interpret the two-motor transport results, we uncover the dynamic motor binding and unbinding that occurs when cargos are driven by two motors.

MATERIALS AND METHODS

The model

Simulations used a Brownian dynamics approach similar to that of (11). The equation of motion for the scaffold is given by

$$\frac{dx(t)}{dt} = \frac{1}{\zeta}\left(\sum_{i=1}^{N} F^{m}_{i,\parallel}(t) + F^{B}(t)\right), \tag{1}$$

where $x(t)$ is the position of the cargo, ζ is the friction coefficient, $F^{m}_{i,\parallel}(t)$is the parallel component of the motor force because of the i^{th} motor, and $F^{B}(t)$ is the random force. The random force was chosen to be Gaussian noise with zero mean and a variance, dictated by the fluctuation-dissipation theorem,

$$<F^{B}(t)> \;=\; 0, \tag{2}$$

$$<F^{B}(t)F^{B}(t')> \;=\; 2k_{\mathrm{B}}\mathrm{T}\zeta\delta(t-t'), \tag{3}$$

where T is the temperature, and k_B is Boltzmann's constant. The friction coefficient for a spherical cargo (23) is given by $\zeta^{s} = 6\pi\eta r$, where r is the radius of the sphere. For a cylinder near a surface, the longitudinal friction coefficient can be written as (23)

$$\zeta^{c} = \frac{2\pi\eta L}{ln(4h/d)}, \tag{4}$$

where L is the length, d is the diameter of the scaffold, and h is the distance between the microtubule and the scaffold. For both friction coefficients, η is the dynamic viscosity of the fluid. The friction coefficient can then be written as

$$\zeta = \begin{cases} \zeta^{s} & , \text{ without scaffold} \\ \zeta^{c} + 2\zeta^{s} & , \text{ with scaffold} \end{cases}, \tag{5}$$

where the single-motor system has only a fluorophore tag attached to the motor tail domain without the scaffold, and the two-motor system has a scaffold and two fluorophore tags. The equation of motion was integrated using an Euler scheme, with a time step of $\tau = 0.1$ μs.

Motors were modeled as a cable-like Hookean springs with zero stiffness up to a rest length, r_0, of 40 nm, and a linear stiffness (κ_s) with 0.2 pN/nm compliance beyond it, as described in (11). Motors in that previous study were truncated at residue 560, identical to the kinesin-1 (kin1) construct used here. The kinesin-3 (kin3) construct is truncated at residue 393 but contains a leucine zipper, and so we approximated it as the same length.

During every time step of the simulation, τ, a motor takes a step stochastically with a probability $p_{step} = 1 - e^{-v\tau/\delta}$, where $\delta = 8$ nm is the motor step size, and v is the motor velocity. For hindering loads, the motors obey a force-velocity curve of the form

$$v \;=\; v_u\left[1 - \left(\frac{F_{\parallel}}{F_s}\right)\right]. \tag{6}$$

Here, $F_{\parallel}$ is the component of the exerted force parallel to the microtubule, v_u is the zero-load motor velocity taken from previous experiments (20,24,25), and $F_s = 7$ pN is the stall force (11,26). For assisting loads, motors move with the unloaded velocity, $v = v_u$.

Load-dependent motor detachment was incorporated, similar to previous simulations (11), with the following modifications. Zero-load motor detachment rates, $k_{off,0}$, for the four motors were calculated by dividing the mean velocity by the mean run length for each motor, with values taken from

previous zero-load single-molecule measurements (20,24,25). Load dependence of detachment for kin1 was based on published optical trapping experiments (26), as fit in (11):

$$k_{off}(F) = \begin{cases} k_{off,0} * e^{\frac{F}{6.1}} & , \text{ hindering direction} \\ k_{off,0} + 1.56 * F & , \text{ assisting direction} \end{cases}, \tag{7}$$

where off rates are in s^{-1}, and force is in pN. For kin3, the load-dependent off rate was symmetric,

$$k_{off}(F) = k_{off,0} e^{\frac{|F|}{F_c}}, \tag{8}$$

with $F_c = 0.5$ pN, chosen based on available experimental data (19), a previous simulation study (11), and a parameter sensitivity scan (see Supporting Materials and Methods, Section S3). It is important to note that, because of thermal fluctuations and the finite time step size in the simulations, we found that recapitulating the experimentally observed unloaded off rates, particularly for a force-sensitive motor such as kin3, requires correcting the zero-load detachment rates empirically (discussed in Supporting Materials and Methods, Section S3). Briefly, if one defines the dimensionless constants $\alpha \equiv \sqrt{\kappa_s k_B T}/F_c$ (ratio of thermal force on the tether spring to critical detachment force) and $\beta \equiv \sqrt{k_B T/\kappa_s (r_0^2 - h^2)}$ (ratio of thermal force on the tether spring to force of the tether), this correction to the leading order can be written as

$$\frac{\langle k_{off,0} \rangle}{k_{off,0}} \approx P_0(\beta) + (1 - P_0(\beta)) e^{\alpha^2/2} \times \left[1 + \sqrt{\frac{2}{\pi}} \left(\alpha - \frac{\alpha^3}{6} + \frac{\alpha^5}{40} \right) \right], \tag{9}$$

where $P_0(\beta) \equiv 1/[\beta\sqrt{\pi/2} + 1]$. Note that in the limit, the temperature goes to zero, and this correction vanishes as expected. For the parameters used in the simulations (Table S1), $\alpha \approx 0.9/F_c$, $\beta \approx 0.12$, and $P_0(\beta) \approx 0.87$. Therefore, for kin1 and kin3, $\alpha \approx 0.15$ and ≈ 1.8, respectively, which in turn yields an expectation value $k_{off,0}$, approximately the same as input $k_{off,0}$ for kin1, and $k_{off,0}$ is nearly a factor of two larger than the input zero-load off rate for kin3 (see Supporting Materials and Methods, Section S3 for further details). As a result, the unloaded off rates for the simulations were chosen as 0.93 s^{-1} for kin1 wild-type (WT) and 0.25 s^{-1} for kin1 swapped (Swap) and 0.24 s^{-1} for kin3WT and 0.37 s^{-1} for kin3Swap (Table S2).

After detachment, the motor reattaches to the microtubule in an unstrained conformation to the microtubule with a force-independent on rate, $k_{reattach}$, which is the free parameter in our simulations.

Cell culture, transfection, and lysis

Plasmids containing kin1, kin3, and the scaffold were triply transfected into COS7 cells as described previously (20). After overnight expression (16 h), the cells were trypsinized and harvested by low-speed centrifugation at 1500 × *g* at 4°C. The pellet was washed once in Dulbecco's modified Eagle's medium and resuspended in 25 μL lysis buffer (25 mM HEPES/KOH, 115 mM potassium acetate, 5 mM sodium acetate, 5 mM $MgCl_2$, 0.5 mM EGTA, and 1% Triton X-100 (pH 7.4)) freshly supplemented with 1 mM ATP, 1 mM phenylmethylsulfonyl fluoride, and protease inhibitors (10 μg/mL leupeptin, 5 μg/mL chymostatin, 3 μg/mL elastatinal, and 1 mg/mL pepstatin). After the lysate was clarified by centrifugation at 16,000 × *g* at 4°C, aliquots were snap-frozen in liquid nitrogen and stored at −80°C.

Total internal reflection fluorescence motility assays

Two-color total internal reflection fluorescence (TIRF) assays were performed as described previously (20,27) at room temperature in a narrow flow cell (~10 μL volume) prepared by attaching a clean #1.5 coverslip to a glass slide with double-sided tape. HiLyte-647-labeled microtubules were polymerized from purified tubulin (Cytoskeleton, Denver, CO) in BRB80 buffer (80 mM PIPES/KOH, 1 mM EGTA, and 1 mM $MgCl_2$ (pH 6.8)) supplemented with 1 mM GTP at 37°C for 15 min. Polymerized microtubules were stored at room temperature after the addition of five volumes of prewarmed BRB80 containing 20 μM taxol and an additional 15 min incubation at 37°C. Polymerized microtubules were diluted in P12 buffer (12 mM PIPES/KOH, 1 mM EGTA, and 2 mM $MgCl_2$, pH 6.8) containing 20 μM taxol and then infused into a flow cell and incubated for 5 min at room temperature to adsorb onto the coverslip. Subsequently, 50 μL of blocking buffer (10 mg/mL bovine serum albumin in P12 buffer with 10 μM taxol) was introduced and incubated for 10 min to prevent nonspecific binding of kinesin motors onto the coverslip surface. Finally, lysates containing motors and scaffolds (typically 0.1–1 μL) were added to the flow chambers in P12 buffer supplemented with 2 mM ATP, 10 mg/mL bovine serum albumin, 10 μM taxol, and oxygen-scavenging components to reduce photobleaching (1 mM dithiothreitol, 1 mM $MgCl_2$, 10 mM glucose, 0.1 mg/mL glucose oxidase, and 0.08 mg/mL catalase). The motility data for each combination were obtained from at least two independent protein preparations.

Image acquisition

Images for TIRF motility assays were acquired on a Nikon Ti-E/B microscope with a 100× 1.49 numerical aperture oil immersion TIRF objective with a 1.5× tube lens (Nikon, Tokyo, Japan) equipped with three 20-mW diode lasers (488, 561, and 640 nm) combined into a single fiber and rapidly controlled with an acousto-optic tunable filter (Agilent Technologies, Santa Clara, CA). Images were collected via an electron multiplying-CCD detector (iXon X3 DU897, 512 × 512, 16 μm array; Andor Technology, Belfast, UK). For near simultaneous, two-color imaging, the microscope was modified to include a dual-band laser polychroic mirror (ZT488/561rpc; Chroma Technology, Bellows Falls, VT), a dual-band sputtered emission filter (ZET488/561m; Chroma Technology), and a dual-band sputtered clean-up filter (ZET488/561x; Chroma Technology), and the acousto-optic tunable filter was used to rapidly switch between 488 nm (2 mW power) and 561 nm (4 mW power) laser excitation with 50 ms exposures in each channel. Images were acquired continuously such that the interval between frames for a single color was 100 ms.

Because of differences in expression levels, 17% of complexes purified from cells contained both motors. This result is not surprising because at low motor expression levels, most scaffolds will have only one motor, and at high motor expression levels, there will be free motors. Because only complexes containing both fluorophores were analyzed, free motors and partially occupied scaffolds did not affect the results. Single-motor off rates were calculated by dividing the mean velocity by the mean run length, and uncertainty was obtained by propagating errors.

Two-color motility analysis

For analysis of kin1 + kin3 motility events, kymograph analysis was performed, essentially as described previously (20). Maximal intensity projections were generated to determine the location of microstubules, and kymographs were generated (width = 5 pixels) along these tracks in both the 488 and 561 nm channel using Elements (Nikon). Two-color events were defined as the area where kymographs in both channels overlapped (i.e., were separated by less than a pixel) and moved together for at least

five frames (500 ms). Any stalled events, (i.e., particles that showed no displacement over five frames) were ignored. Velocity was defined as the displacement of the particle (the vertical component of the kymograph, in micrometers) divided by the observation time for the particle (the horizontal component of the kymograph, in seconds).

Landing rate determination

Motor landing rates (Events/(μm $\times$ min)) were determined by counting the number of motility events and dividing by the observation time, microtubule length, and motor concentration as described previously (25). Time was defined as the recording time (in minutes), and microtubule length was determined by measuring the contour length of the HiLyte-647-labeled microtubule in the 640 nm channel (in micrometers). Equimolar amounts of each motor were added to each flow chamber, in which the motor concentration in each lysate was normalized by quantitative Western blot.

RESULTS

Construction of defined two-motor complexes

To investigate the cooperative transport of cargo by two kinesin motors, we used a system of α-helical scaffolds and protein linkers developed previously (20) to link pairs of motors. The motors were identical to those used in (20). We exploited the high affinity of the superfolder split green fluorescent protein (GFP) (28) and the split EF-hand from calbindin (29) to assemble two-motor assemblies in COS7 cells via protein-protein self-assembly. Cells were triply transfected with three constructs (Fig. 1 *A*): 1) kin1 (amino acids 1–560 of rat KIF5C (30), hereafter referred to as kin1) tagged with mNeonGreen and strand 11 of the GFP barrel; 2) kin3 (amino acids 1–393 of rat KIF1A with the leucine zipper dimerizing segment of GCN4 (24), hereafter referred to as kin3) tagged with 2xmCherry and the C-terminal half of the split EF-hand from calbindin; and 3) a scaffold protein consisting of a SNAP-tagged, 20-nm single α helix (SAH, from *Saccharomyces cerevisiae* mannosyl transferase MNN4 (31)) flanked by the N-terminal half of the split EF-hand for kin3 attachment and strands 1–10 of the GFP barrel for kin1 attachment. After overnight expression, cells were lysed, and the motility of the resulting complexes were analyzed by TIRF microscopy. Single-motor motility parameters were obtained by expressing kin1 and kin3 in the absence of the scaffold and analyzing these cell lysates by TIRF; representative kymographs are shown in Fig. 1 *B*, and velocity and run length values are presented in Fig. 2 and Table S2.

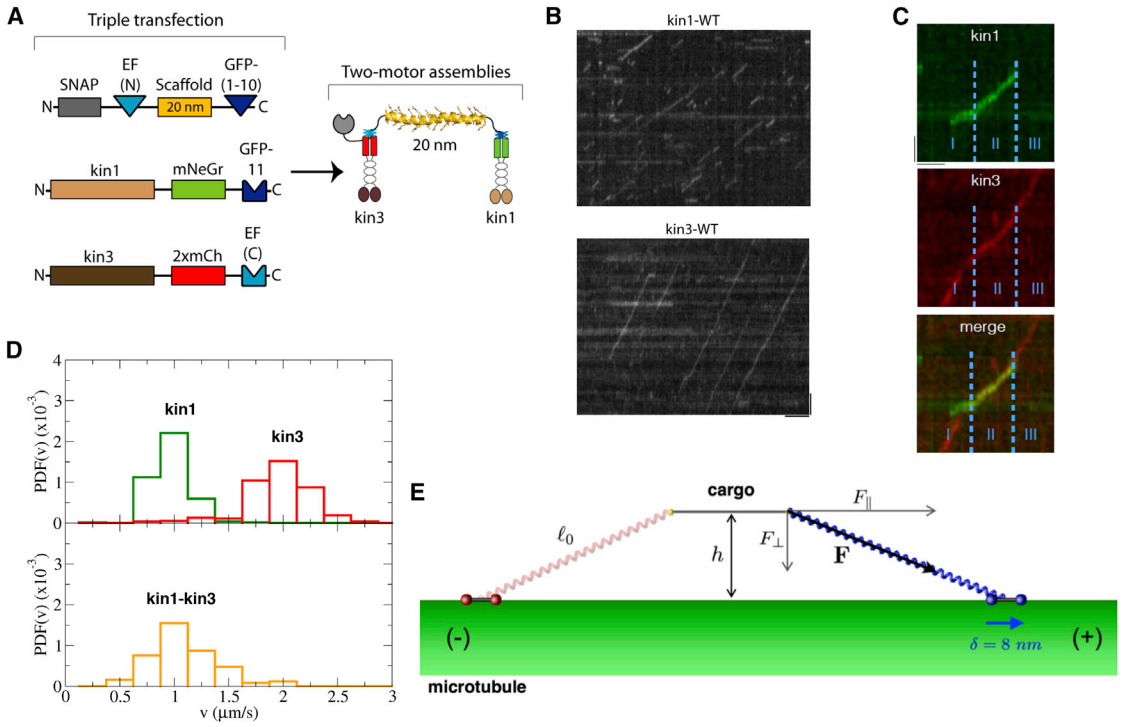

FIGURE 1 Construction and analysis of motor-cargo complexes. (*A*) Motor and scaffold proteins used to generate two-motor complexes. Final complex consists of a single α helix (SAH) scaffold with one kinesin-1 (kin1) and one kinesin-3 (kin3) motor attached. (*B*) Single-motor trajectories were obtained for wild-type (WT) kin1 or kin3 motors without scaffold. Kymographs are oriented as the position on the vertical axis and time on the horizontal axis. Scale bars, 1 μm and 1 s, respectively. (*C*) Trajectories of complexes containing the scaffold, kin1, and kin3 are shown. Regions of two-motor transport were defined as segments of the kymograph in which green (kin1) and red (kin3) spots colocalize (shown as yellow in the merged figure). In segment I, the motors move independently and at different speeds on the microtubule; in segment II, the motors join and move as a complex; and in segment III, the kin1 separates from the kin3 and dissociates from the microtubule. (*D*) Velocity distributions for kin1 alone (*green*), kin3 alone (*red*), and kin1-kin3 complexes (*yellow*) are shown. (*E*) Diagram of the model used for cargo transport simulations is shown; see text for model details. To see this figure in color, go online.

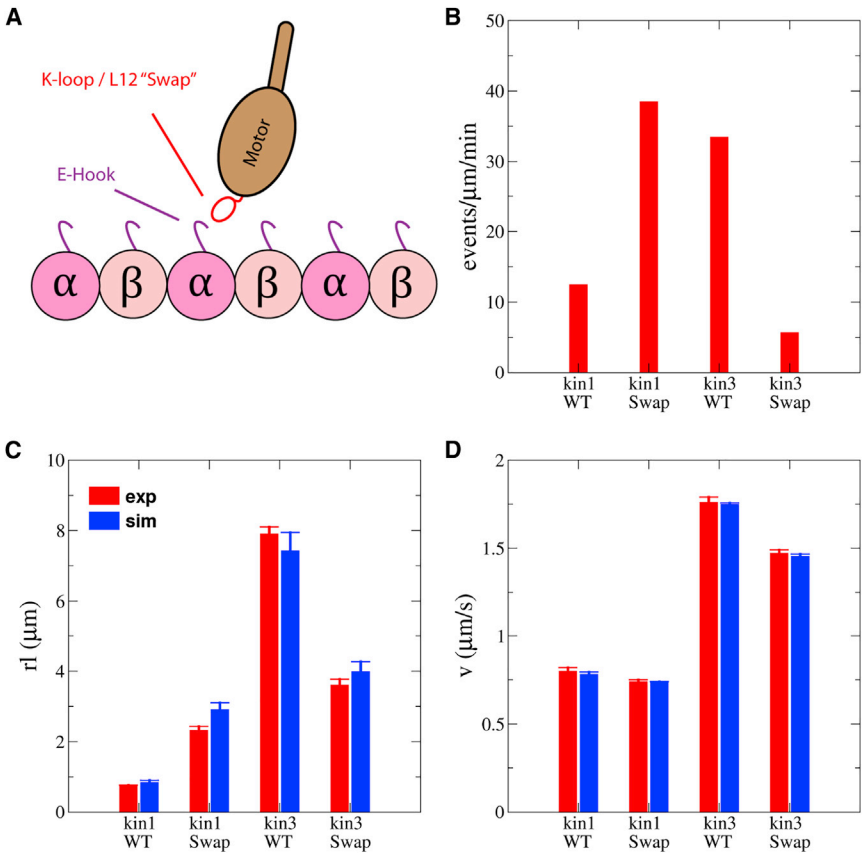

FIGURE 2 Characterization of loop 12 swap mutants. (*A*) Diagram of motor-microtubule binding shows the interaction of the positively charged loop 12 (K-loop) of kin3 with the negatively charged C-terminus (E-hook) of tubulin. WT denotes wild-type. (*B*) Motor landing rates were measured from single-molecule assays, which provide relative bimolecular on-rates for the four motors. (*C* and *D*) Experimental (*red*) and simulated (*blue*) single-motor run lengths (*C*) and velocities (*D*) for all four motors are shown. Error bars are standard error of the mean. WT denotes wild-type. To see this figure in color, go online.

Proper assembly of two-motor complexes was confirmed by observing the coincident movement of red (kin3) and green (kin1) signals along immobilized microtubules (Fig. 1 *C*); this combination of linkers and scaffold resulted in a maximal of 17% red/green colocalization for motile events (20). Because motors stochastically bind and unbind from the microtubule, the movement of kin1-kin3 complexes may result from only one motor being engaged with the microtubule or both motors simultaneously transporting the cargo. Consistent with this dynamic behavior, the distribution of velocities for cargo driven by two-motor complexes is broad (Fig. 1 *D*), and the mean velocity of 969 $\pm$ 293 nm/s lies between the single-motor velocity of kin1 (800 $\pm$ 20 nm/s (20)) and single-motor velocity of kin3 (1760 $\pm$ 30 nm/s (20)). Notably, the mean velocity for cargo cotransported by kin1 and kin3 was much closer to the kin1 velocity, demonstrating that by some combination of faster on rates and slower off rates, kin1 dominates the transport behavior of the kin1-kin3 complexes.

Computational model of cargo transport

To understand the motor-motor interactions underlying multimotor transport, we developed a computational model of cargo transport driven by two kinesin motors. Experimental geometries were mimicked by modeling the microtubule as an immobilized surface and modeling the protein scaffold as a rigid rod of length of 20 nm (20) that lies 15 nm above the surface of the microtubule (32) (Fig. 1 *E*). Inertial effects were neglected, and the cargo was embedded in a solvent modeled using Langevin dynamics and subject to random Brownian forces (11). Motors were attached to the ends of the cargo and modeled as a cable-like Hookean springs with zero stiffness up to a rest length of 40 nm, and a linear stiffness of 0.2 pN/nm beyond this slack length (similar to (11)). Motor stepping and unbinding were modeled as probabilities during each 0.1 μs time step, with values coming from published experimental data, in which the available single-molecule velocity and run lengths for the four motors used in this study were published previously (24,25); unloaded motor off rates ($k_{off,0}$) were calculated from these data by $k_{off,0}$ = velocity/run length (Table S2). The load-dependent off rate for kin1 was taken from published optical trapping experiments, similar to previous work (11,26,33) (see Materials and Methods, also Table S2). The force-dependent detachment rate for kin3 (F_c = 0.5 pN) was chosen based on available experimental data (19), a previous simulation study (11), and a parameter sensitivity scan (described in Supporting Materials and Methods, Section S3). Motor reattachment rates were unknown variables that were constrained by simulation, as described below.

Loop 12 alters motor on rates and run length but not velocity

The motor reattachment rate is an unknown free parameter in this model. This first-order rate constant, $k_{reattach}$, is a product of the intrinsic bimolecular on rate for motor-microtubule binding under these conditions and the effective local concentration of tubulin binding sites, which depends on the geometry of the motor-cargo complex, the stiffness of the motor tether, and potentially other variables. The approach taken here was to experimentally vary the bimolecular on rate and use the resulting changes in motor velocity to tune the model and identify a best fit for $k_{reattach}$. To provide experimental constraints for $k_{reattach}$, mutants were constructed in which the kin3 K-loop was Swap into kin1 and vice versa (Fig. 2 *A*). The positively charged K-loop of kin3 was shown previously to modulate the on rate for motor binding, consistent with an electrostatic component of microtubule binding (25). To confirm that swapping loop 12 altered motor on rates, single-molecule assays were carried out and the number of landing events per micron of microtubule per unit time was measured for the four constructs. As shown in Fig. 2 *B*, the differences in microtubule binding rates between kin1 and kin3 could be fully accounted for by their different loop 12 sequences. Importantly, the data in Fig. 2 *B* provide relative microtubule reattachment rates for the four motors that can be used as constraints for the simulations. However, the absolute first-order reattachment rates, which incorporate effective local concentrations that are determined by the geometry of the system, are unknowns and thus are free parameters in the simulations.

Single-motor run lengths were also altered by swapping loop 12, with the kin3 K-loop enhancing run length for both motors (Fig. 2 *C*). In contrast, motor velocities were unaffected by the loop 12 swaps (Fig. 2 *D*), consistent with previous work (31). Both of these results are consistent with the positively charged K-loop in kin3 acting as an electrostatic tether to enhance motor-microtubule interaction in a manner that does not measurably increase the drag coefficient of the motor along the microtubule. Finally, from the velocity and run length values for each motor, first-order motor off rates in the absence of load were calculated as described above (Table S2).

These motor parameters were input into simulations for the transport of cargo by a single kin1 or kin3 motor. These single-motor simulations (described in Materials and Methods) recapitulated the motor velocity and run lengths for all four constructs (Fig. 2, *C* and *D*), confirming that the velocity and unloaded off rate parameters are appropriate. However, it should be noted that the single-motor results say nothing about the load dependence of the off rate nor the motor reattachment rate of the different motors, because these parameters do not come into play in these single-motor simulations.

Simulations match average multimotor velocities

Having confirmed that single-motor simulations recapitulate the experimental data, we turned to the case of cargo cotransport by one kin1 and one kin3 motor. Experimental velocity distributions for the four pairs of motors (kin1 and kin3 with either WT or Swap loop 12 domains) are shown in Fig. 3, *A–D*. To understand the underlying motor-motor coordination, simulations were carried out using parameters taken from the one-motor simulations. To minimize the number of free parameters, the motor reattachment rate was set to infinitely high for these initial simulations, meaning that motors that detach from the microtubule instantaneously reattach so long as the other motor is tethering the cargo to the microtubule. Simulated velocity distributions were compared to experimental distributions (plotted as cumulative distribution in Fig. 3, *A–D* main panels and probability distributions in insets), and mean velocity and SD for each case were also compared (Fig. 3, *E* and *F*). As shown, the model simulations accurately reproduced the mean cargo velocity for different motor pairs (Fig. 3 *E*). However, the widths of the velocity distributions differed (Fig. 3, *A–D*); this is shown quantitatively as differences in the velocity SDs in Fig. 3 *F*.

We next explored the degree to which the simulation results are dependent on parameter choices for the load-dependent detachment of kin3. A strength of this study is that the unloaded velocities and off rates are experimentally constrained, and published data are available to describe the load dependence of kin1 detachment. In contrast, there are limited experimental constraints for the load-dependent off rate of kin3. In previous modeling of multimotor microtubule gliding behavior, we used existing experimental constraints of the kin1 and kin2 load-dependent off rates to estimate the sensitivity of kin3 motors to load (10). The critical detachment force of $F_c = 0.5$ pN from that work (in which $k_{off}(F) = k_{off,0}e^{|F|/F_c}$, also known as Bell's law) implies that even small external loads significantly increase the motor detachment rate. Available experimental data on this question are consistent with the following: Tomishige and co-workers found that an ~1.5 pN load led to roughly a 10-fold increase in the Unc104/KIF1A detachment rate, consistent with $F_c = 0.65$ pN (Fig. S2 *E* of (19)). To determine the dependence of the simulation results on kin3 load-dependent detachment, we varied $k_{off,0}$ and F_c for kin3 and calculated the average sum-squared error for the four motor pairs. There was a clear minimal at $F_c = 0.5$ pN (Fig. S3), which provides independent evidence for a strong load dependence of kin3 detachment.

Parameter scanning identifies best fit for motor attachment rate

Although the simulations captured the mean two-motor velocities, the discrepancy in the widths between the simulated and experimental velocity distributions remained. The first potential explanation is that the relatively wide two-motor

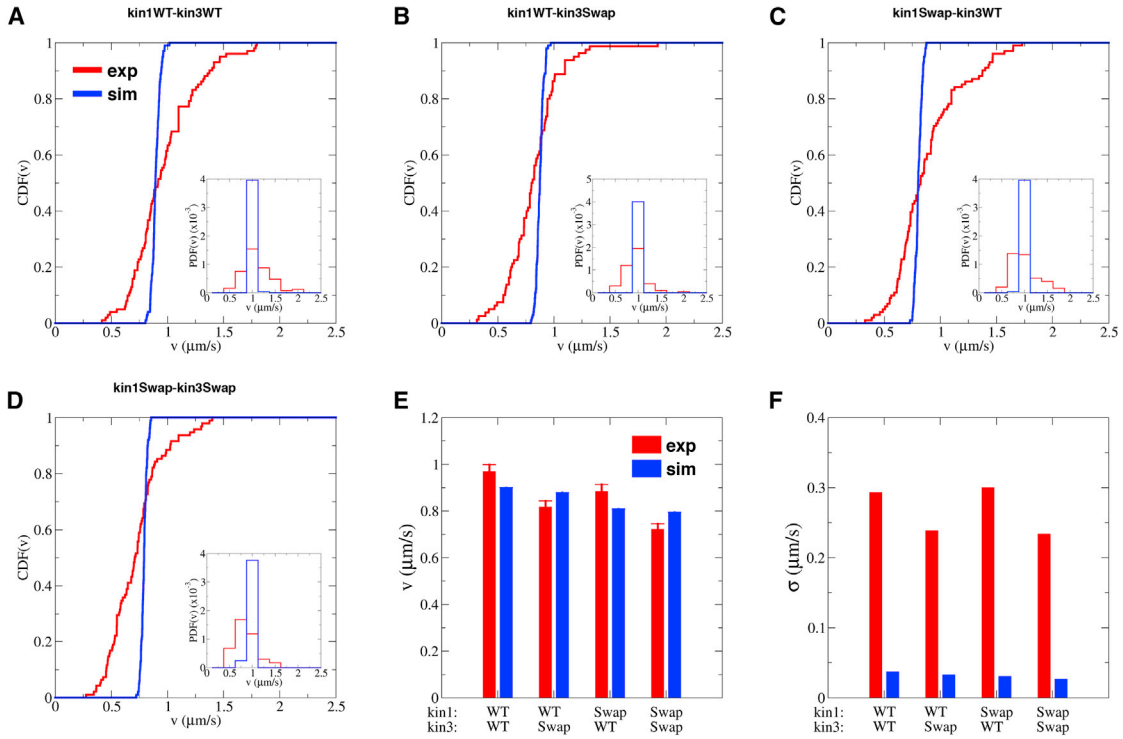

FIGURE 3 Comparing experimental velocities to model results with instantaneous motor reattachment. (*A–D*) Cotransport velocities for different motor pairs are shown, comparing experimental (*red*) to simulated (*blue*). Cumulative velocity distributions are shown for (*A*) kin1WT-kin3WT, (*B*) kin1WT-kin3Swap, (*C*) kin1Swap-kin3WT, and (*D*) kin1Swap-kin3Swap pairs. Insets show probability distributions for each. (*E* and *F*) Comparison of (*E*) velocity (error bars are standard error of the mean) and (*F*) SD of velocity for different motor pairs, which show the failure of simulation using instantaneous motor reattachment rates to recapitulate experimental data. To see this figure in color, go online.

velocity distributions (Fig. 1 *D*) are simply a consequence of the single-motor velocity distributions, which are wider than would be predicted from a simple Poisson stepper (34). To test this possibility, we reran simulations but used the single-motor velocity distributions in Fig. 1 *D* to set the mean single-motor velocity for each run. Although this modification did increase the width of the two-motor velocity distributions, it could not capture the full width of the experimentally observed distribution (Fig. S4).

The second possibility to account for widths of the two-motor velocity distributions is that, because of finite motor reattachment rates, the experimental trajectories include periods in which only one motor is attached to the microtubule, and the cargo is moving at either the faster single-molecule kin3 velocity or the slower kin1 velocity. This behavior, which would be expected to broaden the two-motor velocity distribution, is not captured in simulations in which motors that detach instantaneously reattach to the microtubule. Although the single-molecule landing rates in Fig. 2 *B* provide experimental constraints for the relative bimolecular on rates for the various loop 12 swaps, the absolute microtubule reattachment rates for cargo-attached motors that unbind from the microtubule are not known. Thus, simulations were run using a range of values for reattachment rate for WT kin1 ($k_{\text{reattach}}^{\text{kin1WT}}$); the other reattachment rates were scaled based on the relative bimolecular on rates in Fig. 2 *B*, leaving only one free parameter. For each motor pair, simulations were carried out across different values of $k_{\text{reattach}}^{\text{kin1WT}}$, and velocities were compared by taking the ratio of the mean (Fig. 4 *A*) and SD (Fig. 4 *B*) of experimental and simulated velocities. As shown in Fig. 4 *A*, the simulated mean velocities matched reasonably well for $k_{\text{reattach}}^{\text{kin1WT}}$ of 3 s^{-1} or greater. In contrast, the simulated SDs significantly underestimated the experimental observations for values of $k_{\text{reattach}}^{\text{kin1WT}} > 3\ s^{-1}$ (more than 20% error). A χ-squared analysis performed on the overall shape of the distributions came to a similar conclusion (see Supporting Materials and Methods, Section S5). Based on these analyses, we chose $k_{\text{reattach}}^{\text{kin1WT}} = 3\ s^{-1}$ and scaled the other rates based on the relative landing rates shown in Fig. 2 *B*, resulting in $k_{\text{reattach}}^{\text{kin1Swap}} = 9.28\ s^{-1}$, $k_{\text{reattach}}^{\text{kin3WT}} = 8.06\ s^{-1}$, and $k_{\text{reattach}}^{\text{kin3Swap}} = 1.36\ s^{-1}$.

When motor reattachment rates were adjusted, the simulations were able to reasonably recapitulate the experimental velocity distributions (Fig. 5). As shown in Fig. 5 *E*, the mean velocities from the simulations are all within 17% of their experimental values, with an average difference of 11%. The SDs of the simulated velocity distributions in Fig. 5 *F* also matched the experimental values reasonably well, particularly for pairs containing kin1WT motors.

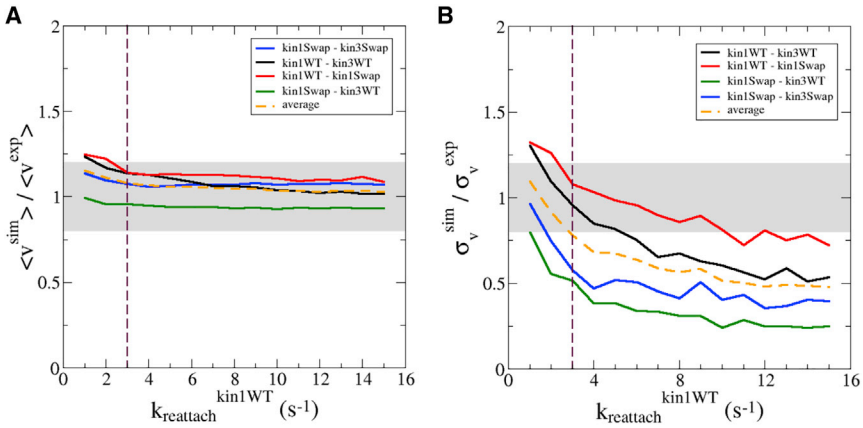

FIGURE 4 Parameter sensitivity analysis for motor reattachment rate. Reattachment rates were constrained to be proportional to $k_{reattach}^{kin1WT}$ based on experiments, and velocity distributions were produced across a range of $k_{reattach}^{kin1WT}$ and compared to experimental distributions. (*A*) The ratio of simulated and experimental mean velocity shows the deviation in simulations for lower reattachment rates. (*B*) The ratio of simulated and experimental SD of velocity shows significant differences between the two for higher reattachment rates. From the mean velocity and SD ratios, a value of $k_{reattach}^{kin1WT} = 3\ s^{-1}$ was chosen as the compromise for subsequent simulations, and other reattachment parameters were scaled according to Fig. 2 *B*. Gray shaded region represents ±20% difference. Orange dashed line shows the average of the relevant ratio across all motor combinations. To see this figure in color, go online.

Simulated SDs were within 26% of their experimental values on average, which contrasts with an average error of 88% on the SD when an infinite on rate was used (Fig. 2 *F*). It is important to note that in this optimization, a single parameter was varied in an effort to match four independent experimental data sets. Thus, although the model could be made more complex in an effort to further improve the average errors, we chose to stay with a minimalistic model and used it to gain physical insight into motor dynamics underlying the observed transport.

Simulations reveal dynamic motor behavior underlying cargo cotransport

Having tuned the model parameters using experimental constraints, we used the simulations to investigate the

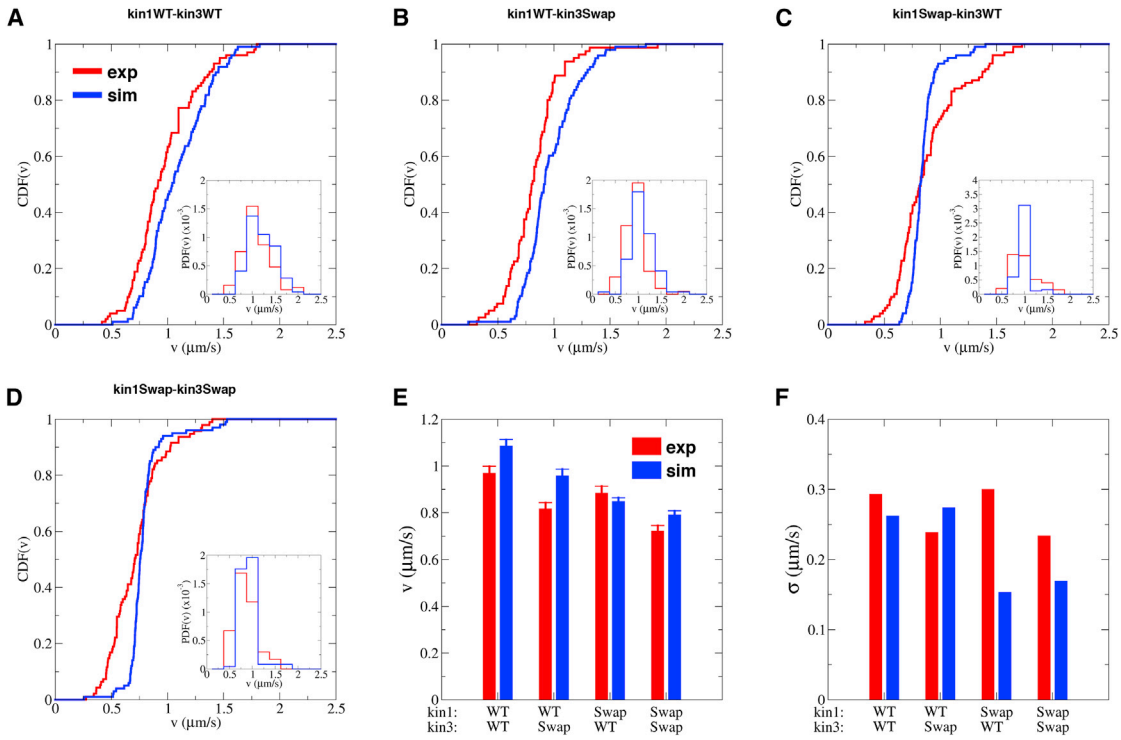

FIGURE 5 Velocity distributions using model-optimized motor reattachment rates. (*A–D*) Cumulative velocity distributions for motor pairs (*A*) kin1WT-kin3WT, (*B*) kin1WT-kin3Swap, (*C*) kin1Swap-kin3WT, and (*D*) kin1Swap-kin1Swap. Insets show probability distributions for each. (*E*) Mean transport velocities for different motor pairs are shown, comparing experimental (*red*) to simulated (*blue*) data. Error bars are mean ± SE. (*F*) Comparison of SD of velocity, σ, for different motor pairs is shown. Motor reattachment rates used were $k_{reattach}^{kin1WT} = 3.00\ s^{-1}$, $k_{reattach}^{kin1Swap} = 9.28\ s^{-1}$, $k_{reattach}^{kin3WT} = 8.06\ s^{-1}$, and $k_{reattach}^{kin3Swap} = 1.36\ s^{-1}$. To see this figure in color, go online.

underlying motor dynamics during cargo transport by pairs of kin1 and kin3 motors. As shown in the trajectory in Fig. 6 *A*, transport involves durations in which either motor alone or both motors together are bound to the microtubule, with the dynamics determined by the motor on and off rates. The forces on each motor during transport are shown in Fig. 6 *A* (*lower panel*, see also Fig. S6). When only one motor is bound, the drag force on the attached motor is minimal, and hence, forces for both motors (aside from thermal forces) are zero. When both motors are bound to the microtubule, the slower kin1 motors are predominantly under assisting loads (*green traces*, negative forces), whereas the faster kin3 motors are predominantly under hindering loads (*red traces*, positive forces). Because of the minimal drag forces on the cargo, a force balance is effectively maintained at all times, such that forces when both motors are engaged are of equal magnitude and opposite direction.

The influence of motors on one another can be seen by the decrease in association time (inverse of motor off rate) in Fig. 6 *B*. Interestingly, because of its high sensitivity to load, the mean association times of kin3 are reduced between 87 and 97% when paired with kin1, whereas kin1 association times are reduced only in the range of 32–62%. For instance, when paired with kin1WT, the kin3WT residence time decrease from 4.0 to 0.23 s, whereas the kin1WT residence time decreases from 1.08 to 0.67 s (see Fig. S6). These results demonstrate the principle that kin3 motors rapidly detach, re-equilibrate their position near the cargo, and reattach, whereas kin1 motors continue to pull. This behavior can be seen in the similarity of the mean motor velocities to their unloaded values in Fig. 6 *C*. For kin1, this results from the property that assisting loads do not increase the single-motor velocity (26). For kin3, this fast average velocity during cargo transport results from the time it takes for kin3 to pull the cargo tether taut; when intermotor forces that slow velocity build up, the motor detachment rate rises sharply, resulting in motor detachment.

The influence of intermotor forces can be investigated further by examining the mean force at the instant of detachment (Fig. 6 *D*). Kin3 motors in the two-motor simulations tend to detach at positive (hindering) forces in the range of 3–4 pN, whereas kin1 detached at assisting forces of 0.3–1.5 pN (Fig. 6 *D*). Because the kin3 off rate depends strongly on load, the higher detachment forces for this motor seem paradoxical but can be understood by considering that for kin3WT, the unloaded stepping rate is 218 s^{-1}, whereas the unloaded off rate is only 0.24 s^{-1}. Thus, when two motors start near one another, the faster kin3 needs to first pull out the slack of the tether (moving at its unloaded velocity) and then build up force (which occurs rapidly because of the

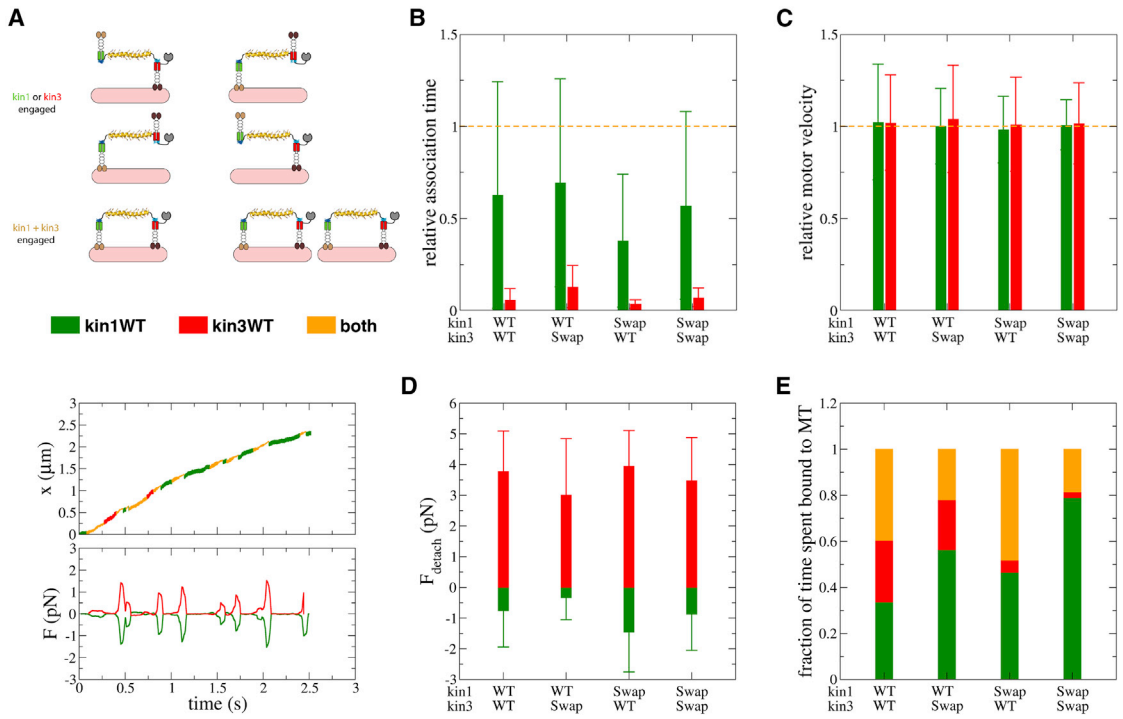

FIGURE 6 Simulations of cargo transport by pairs of wild-type kin1 and kin3 motors. (*A*) Simulated trajectory shows the regions of wild-type kin1 only (*red*), kin3 only (*green*), and both motors attached (*yellow*). Lower panel shows instantaneous forces on each motor during transport, smoothed using a 50 ms boxcar average. (*B*) Mean association times (relative to the unloaded motor association time) for each motor in the complex are shown. (*C*) Mean motor velocities (relative to the unloaded motor velocities) during cotransport of cargo are shown. (*D*) Mean force at the moment of detachment from the microtubule is shown. (*E*) The fraction of time spent in states with one or two motors bound for simulations for the four motor combinations is shown. Error bars are SDs. Raw data for (*B* and *C*) are shown in Fig. S6 and Table S2. Additional force trajectories are shown in Fig. S7. To see this figure in color, go online.

fast motor speed and 0.2 pN/nm stiffness of the extended tether). Hindering forces slow the velocity while speeding up detachment, such that the stepping rate and detachment rate are matched around 3 pN of hindering load, which is right in the range of the mean detachment force for kin3.

Finally, plotting the proportion of time the cargo is transported by either motor or both motors for the different motor pairs reveals a number of features (Fig. 6 *E*). First, with the on (reattachment) and off rates used here, the cargo is transported by the actions of both motors for less than half of the time for all motor combinations. Second, for WT motors, the time spent with only one kin1 attached is similar to the time spent with only one kin3 attached, meaning that the faster on rate of kin3 because of its K-loop is offset by its greater propensity to detach under load. Third, enhancing the kin1 reattachment rate by swapping in the kin3 K-loop reduces the time the motor is transported by only kin3 to nearly zero, again emphasizing the importance of the K-loop in modulating motor dynamics.

DISCUSSION

In a number of documented cases, intracellular cargos are transported by teams of kinesins from different families possessing different unloaded transport velocities (3,4,8,9). It has been suggested that this teamwork enables the cargo to be carried along diverse microtubule tracks that have different post-translational modifications or microtubule-associated proteins bound or to better traverse roadblocks (7). However, teaming motors with different velocities inherently sets up a competition between the motors, the outcome of which is influenced by many factors including the following: 1) the force-velocity relationship for each motor class, 2) the sensitivity of each motor to detachment under load, 3) the reattachment rate of each motor, and 4) the stiffness of the cargo. Experimental dissection of this problem is hampered by the difficulty of defining periods of single versus cotransport in which either one or both motors, respectively, are actually attached to the microtubule and exerting pulling forces. The approach taken here was to develop a simple cargo transport model based on published characteristics of kinesin-1 and kinesin-3 motors, to use experiments to constrain unknown parameters in the model, and to use the model to describe the underlying motor dynamics that determine the observed cargo transport behavior.

Consistent with previous work (3,11,20), we found that transport speeds of cargo cotransported by kinesin-1 and kinesin-3 motors are much closer to the kinesin-1 speeds, suggesting that kinesin-1 dominates transport. The first motor property that determines this behavior is the asymmetric kinesin force-velocity curve—although hindering loads slow motors down, assisting loads do not speed motors up (26,35). Thus, a fast cargo velocity requires some combination of stretching compliant linkages between motors and/or slower motors detaching as a result of load. The second property that determines cotransport speed is the propensity of motors to detach under load. From the available evidence, which is supported by parameter scans carried in this study (Fig. S3), kinesin-3 detaches more readily under load than kinesin-1 (11,19,20). Both the force-velocity asymmetry and the load-dependent detachment properties favor kinesin-1. However, a third and understudied factor is the rate of motor reattachment to the microtubule after dissociation. On one extreme, slow reattachment sets up a scenario in which the cargo is usually being carried by only one motor (or motor class). At the other extreme, an infinitely fast reattachment rate means that all motors are simultaneously transporting the cargo and the stretching of the linkages will play a key role.

In this work, we took advantage of a discrete domain of kinesin, loop 12, to generate motors with similar unloaded velocities but different microtubule on rates. For both kinesin-1 and kinesin-3 motors, having the positively charged kinesin-3 K-loop increased the influence of that motor on the resulting cargo transport rate, demonstrating the importance of the motor on rate. In addition, the predicted distributions of transport velocities from the model were inconsistent with the data if an infinitely high on rate was assumed, again demonstrating the importance of the reattachment rate. By iterating on $k_{reattach}$, a best fit for this parameter was estimated for each motor, adding the final constraint to the model. With all of the model parameters in hand, we then used the simulations to uncover the motor dynamics underlying the cargo cotransport by kinesin-1 and kinesin-3 motors. The simple story is that kinesin-1 remains on the microtubule for longer durations and dominates the cotransport speed, whereas kinesin-3 frequently detaches because of intermotor tension buildup but rapidly reattaches to the microtubule. This behavior points to the role of kinesin-3 in multimotor transport in maintaining association of the cargo with the microtubule during long distance transport. Because of its fast on and off kinetics, kinesin-3 is expected to be minimally hindered by roadblocks such as microtubule-associated protein or other cargo on the microtubule, which would enhance the overall transport efficiency.

An important finding here was the estimate for $k_{reattach}$ for a scaffold with a defined geometry consisting of a 20 nm SAH domain with motors attached to each end (Fig. 1 *A*). A $k_{reattach}$ value of 5 s^{-1} has been widely used as the motor reattachment rate in multimotor transport based on an estimate from a published model (22), but experimental support for this value has been scant. The estimate of 3 s^{-1} for kin1 and 8 s^{-1} for kin3 derived here by obtaining the best fit of modeled velocity distributions to experiments nicely bracket this value. A recent study that used DNA origami to make defined two-motor assemblies estimated a reattachment rate of 4.4 s^{-1} for kinesin-1 and 16.1 s^{-1} for kinesin-2 (36). It should be noted that $k_{reattach}$ is expected to depend on

the motor-scaffold geometry, so caution should be used in extrapolating this value up to vesicle cargo, such as those carried by kinesin-1 and kinesin-3 in cells. Interestingly, this 3 s^{-1} rate for kinesin-1 is significantly lower than would be expected based on simple geometrical arguments, as follows. Bimolecular on rates of kinesins have been experimentally measured in the range of 3 μM^{-1} s^{-1} using stopped flow (36–38). If we 1) model the protein scaffold and the coiled coil, linker, and GFP regions of the motors together as a compliant 100 nm tether connecting the two pairs of motor domains and 2) postulate that the motor can interact with the six top-most protofilaments on the immobilized microtubule, then the effective tubulin concentration for the 150 tubulin dimers in this 100-nm radius hemisphere is 125 μM. Multiplying this concentration by the bimolecular on rate gives a first-order on rate for the tethered motor binding to the microtubule of 375 s^{-1}, two orders of magnitude greater than the $k_{reattach}$ value estimated here. The reason for this discrepancy is not clear, but it most likely results from geometrical factors that reduce the effective on rate, such as the stiffness of the scaffold, motor-scaffold conformations that disfavor motor binding, and the nonzero volume of the scaffold. The geometrical factors that determine the motor reattachment rates for more physiological cargo are a pressing topic for future work.

It is also important to note the fast detachment rate of force-sensitive motors, such as kinesin-3, provide additional challenges in simulations. Our numerical results, confirmed by our analytical calculations (see Supporting Materials and Methods, Section S3), show that for a motor with a low critical detachment force (such as kinesin-3), the effective zero-load off rate can be significantly modified because of the finite time step size of the simulations and Bell's law detachment. For instance, whereas a motor like kinesin-1 is not significantly affected, the observed zero-load off rate for a force-sensitive motor like kinesin-3 is about a factor of two higher (Fig. S2). This correction is strongly dependent on the dimensionless ratio $\alpha \equiv \sqrt{\kappa_s k_B T}/F_c$ (see Supporting Materials and Methods for details), and can be understood as the ratio of the work done by the motor spring with compliance κ_s—as it goes through a conformational change under force—to thermal energy k_BT. Therefore, care should be taken in similar Langevin dynamics simulations with Bell's law type detachments, in particular when the molecule in question is force sensitive.

This work provides insights into how motors with identical directionalities but different velocities work together to transport cargo. Our results suggest a model of kinesin-1/kinesin-3 cotransport in which kinesin-1 is the dominant transport motor, whereas kinesin-3 rapidly detaches and reattaches, acting both as a tether that enhances association of the cargo with the microtubule and as a motor for stepping around roadblocks on the microtubule. A complete understanding of bidirectional cargo transport in axons and dendrites requires extending these in vitro investigations to teams of kinesin and dynein motors and characterizing the underlying detachment and reattachment rates that determine the net transport speed and directionality of cargo in cells.

SUPPORTING MATERIAL

Supporting Materials and Methods, seven figures, and two tables are available at http://www.biophysj.org/biophysj/supplemental/S0006-3495(19)30106-7.

AUTHOR CONTRIBUTIONS

G.A. developed the simulations. S.R.N. performed the experiments. G.A. and S.R.N. analyzed data, prepared the figures. S.I.M. performed the analytical mean zero-load off rate calculations. V.S. performed the on rate determinations. E.T., K.J.V., and W.O.H. designed and supervised the research. All authors contributed to the writing of the manuscript.

ACKNOWLEDGMENTS

We thank Penn State Research Computing and Cyberinfrastructure for computing time. This work was supported by National Institutes of Health grants R01GM100076 and R01GM121679 to W.O.H. and E.T. and R01GM070862 to K.J.V.

SUPPORTING CITATIONS

References (11,19,20,25) appear in the Supporting Material.

REFERENCES

1. Hirokawa, N., S. Niwa, and Y. Tanaka. 2010. Molecular motors in neurons: transport mechanisms and roles in brain function, development, and disease. *Neuron.* 68:610–638.
2. Encalada, S. E., and L. S. Goldstein. 2014. Biophysical challenges to axonal transport: motor-cargo deficiencies and neurodegeneration. *Annu. Rev. Biophys.* 43:141–169.
3. Encalada, S. E., L. Szpankowski, …, L. S. Goldstein. 2011. Stable kinesin and dynein assemblies drive the axonal transport of mammalian prion protein vesicles. *Cell.* 144:551–565.
4. Hendricks, A. G., E. Perlson, …, E. L. Holzbaur. 2010. Motor coordination via a tug-of-war mechanism drives bidirectional vesicle transport. *Curr. Biol.* 20:697–702.
5. Ligon, L. A., M. Tokito, …, E. L. Holzbaur. 2004. A direct interaction between cytoplasmic dynein and kinesin I may coordinate motor activity. *J. Biol. Chem.* 279:19201–19208.
6. van Spronsen, M., M. Mikhaylova, …, C. C. Hoogenraad. 2013. TRAK/Milton motor-adaptor proteins steer mitochondrial trafficking to axons and dendrites. *Neuron.* 77:485–502.
7. Hancock, W. O. 2014. Bidirectional cargo transport: moving beyond tug of war. *Nat. Rev. Mol. Cell Biol.* 15:615–628.
8. Snow, J. J., G. Ou, …, J. M. Scholey. 2004. Two anterograde intraflagellar transport motors cooperate to build sensory cilia on C. elegans neurons. *Nat. Cell Biol.* 6:1109–1113.
9. Milic, B., J. O. L. Andreasson, …, S. M. Block. 2017. Intraflagellar transport velocity is governed by the number of active KIF17 and KIF3AB motors and their motility properties under load. *Proc. Natl. Acad. Sci. USA.* 114:E6830–E6838.
10. Larson, A. G., E. C. Landahl, and S. E. Rice. 2009. Mechanism of cooperative behaviour in systems of slow and fast molecular motors. *Phys. Chem. Chem. Phys.* 11:4890–4898.

11. Arpağ, G., S. Shastry, …, E. Tüzel. 2014. Transport by populations of fast and slow kinesins uncovers novel family-dependent motor characteristics important for in vivo function. *Biophys. J.* 107:1896–1904.
12. Ally, S., A. G. Larson, …, V. I. Gelfand. 2009. Opposite-polarity motors activate one another to trigger cargo transport in live cells. *J. Cell Biol.* 187:1071–1082.
13. Driver, J. W., A. R. Rogers, …, M. R. Diehl. 2010. Coupling between motor proteins determines dynamic behaviors of motor protein assemblies. *Phys. Chem. Chem. Phys.* 12:10398–10405.
14. Furusawa, H., T. Ozeki, and Y. Okahata. 2006. Observation of DNA conformation changes by energy dissipation measurements on a quartz-crystal oscillator. *Nucleic Acids Symp. Ser. (Oxf).* 50:321–322.
15. Kunwar, A., M. Vershinin, …, S. P. Gross. 2008. Stepping, strain gating, and an unexpected force-velocity curve for multiple-motor-based transport. *Curr. Biol.* 18:1173–1183.
16. Korn, C. B., S. Klumpp, …, U. S. Schwarz. 2009. Stochastic simulations of cargo transport by processive molecular motors. *J. Chem. Phys.* 131:245107.
17. Miki, H., Y. Okada, and N. Hirokawa. 2005. Analysis of the kinesin superfamily: insights into structure and function. *Trends Cell Biol.* 15:467–476.
18. Okada, Y., and N. Hirokawa. 2000. Mechanism of the single-headed processivity: diffusional anchoring between the K-loop of kinesin and the C terminus of tubulin. *Proc. Natl. Acad. Sci. USA.* 97:640–645.
19. Tomishige, M., D. R. Klopfenstein, and R. D. Vale. 2002. Conversion of Unc104/KIF1A kinesin into a processive motor after dimerization. *Science.* 297:2263–2267.
20. Norris, S. R., V. Soppina, …, K. J. Verhey. 2014. A method for multiprotein assembly in cells reveals independent action of kinesins in complex. *J. Cell Biol.* 207:393–406.
21. Rogers, A. R., J. W. Driver, …, M. R. Diehl. 2009. Negative interference dominates collective transport of kinesin motors in the absence of load. *Phys. Chem. Chem. Phys.* 11:4882–4889.
22. Müller, M. J., S. Klumpp, and R. Lipowsky. 2008. Tug-of-war as a cooperative mechanism for bidirectional cargo transport by molecular motors. *Proc. Natl. Acad. Sci. USA.* 105:4609–4614.
23. Howard, J. 2001. Mechanics of Motor Proteins and the Cytoskeleton. Sinauer Associates, Inc., Sunderland, MA.
24. Soppina, V., S. R. Norris, …, K. J. Verhey. 2014. Dimerization of mammalian kinesin-3 motors results in superprocessive motion. *Proc. Natl. Acad. Sci. USA.* 111:5562–5567.
25. Soppina, V., and K. J. Verhey. 2014. The family-specific K-loop influences the microtubule on-rate but not the superprocessivity of kinesin-3 motors. *Mol. Biol. Cell.* 25:2161–2170.
26. Andreasson, J. O., B. Milic, …, S. M. Block. 2015. Examining kinesin processivity within a general gating framework. *eLife.* 4:e07403.
27. Norris, S. R., M. F. Núñez, and K. J. Verhey. 2015. Influence of fluorescent tag on the motility properties of kinesin-1 in single-molecule assays. *Biophys. J.* 108:1133–1143.
28. Cabantous, S., T. C. Terwilliger, and G. S. Waldo. 2005. Protein tagging and detection with engineered self-assembling fragments of green fluorescent protein. *Nat. Biotechnol.* 23:102–107.
29. Lindman, S., I. Johansson, …, S. Linse. 2009. Green fluorescence induced by EF-hand assembly in a split GFP system. *Protein Sci.* 18:1221–1229.
30. Cai, D., K. J. Verhey, and E. Meyhöfer. 2007. Tracking single Kinesin molecules in the cytoplasm of mammalian cells. *Biophys. J.* 92:4137–4144.
31. Sivaramakrishnan, S., B. J. Spink, …, J. A. Spudich. 2008. Dynamic charge interactions create surprising rigidity in the ER/K alpha-helical protein motif. *Proc. Natl. Acad. Sci. USA.* 105:13356–13361.
32. Kerssemakers, J., J. Howard, …, S. Diez. 2006. The distance that kinesin-1 holds its cargo from the microtubule surface measured by fluorescence interference contrast microscopy. *Proc. Natl. Acad. Sci. USA.* 103:15812–15817.
33. Andreasson, J. O., S. Shastry, …, S. M. Block. 2015. The mechanochemical cycle of mammalian kinesin-2 KIF3A/B under load. *Curr. Biol.* 25:1166–1175.
34. Reddy, B. J. N., S. Tripathy, …, S. P. Gross. 2017. Heterogeneity in kinesin function. *Traffic.* 18:658–671.
35. Carter, N. J., and R. A. Cross. 2005. Mechanics of the kinesin step. *Nature.* 435:308–312.
36. Feng, Q., K. J. Mickolajczyk, …, W. O. Hancock. 2018. Motor reattachment kinetics play a dominant role in multimotor-driven cargo transport. *Biophys. J.* 114:400–409.
37. Hackney, D. D. 1995. Highly processive microtubule-stimulated ATP hydrolysis by dimeric kinesin head domains. *Nature.* 377:448–450.
38. Chen, G. Y., D. F. Arginteanu, and W. O. Hancock. 2015. Processivity of the kinesin-2 KIF3A results from rear head gating and not front head gating. *J. Biol. Chem.* 290:10274–10294.

Biophysical Journal, Volume *116*

Supplemental Information

Motor Dynamics Underlying Cargo Transport by Pairs of Kinesin-1 and Kinesin-3 Motors

Göker Arpağ, Stephen R. Norris, S. Iman Mousavi, Virupakshi Soppina, Kristen J. Verhey, William O. Hancock, and Erkan Tüzel

S1 Model Parameters

Table S1. Input parameters used in simulations. Force dependent velocity, $v(F)$, and microtubule detachment rate, $k_{\text{off}}(F)$ have forces shown in units of pN. Microtubule reattachment rates, k_{reattach}, are force-independent. *Velocities, as shown below, have linear force dependency in the hindering direction, and are set to zero beyond the stall force, $F_s = 7\ pN$. In the assisting direction, velocities are constant with values of zero-load velocity as indicated in the table. **kin1WT and kin1Swap have a linear force-dependence in the assisting direction, i.e., $k_{\text{off}}(F) = 1 + 1.56F\,s^{-1}$ and $k_{\text{off}}(F) = 0.2 + 1.56F\,s^{-1}$, respectively, with forces in units of pN (Ref. [1]).

Motor specific parameters			
Motor/Parameter	$\mathbf{v(F)}$ **(nm/s)** *	$\mathbf{k_{off}(F)}$ $\mathbf{(s^{-1})}$	$\mathbf{k_{reattach}}$ $\mathbf{(s^{-1})}$
kin1WT	$800 \times [1 - (F/7)]$	$1.0\ e^{-F/6.1}$ **	3.00
kin1Swap	$740 \times [1 - (F/7)]$	$0.2\ e^{-F/6.1}$ **	9.28
kin3WT	$1760 \times [1 - (F/7)]$	$0.1\ e^{\lvert F\rvert/0.5}$	8.06
kin3Swap	$1470 \times [1 - (F/7)]$	$0.17\ e^{\lvert F\rvert/0.5}$	1.36
Other parameters			
cargo length, L	$20\,nm$	dynamic viscosity, η	$0.002\,Pa \cdot s$
cargo diameter, d	$0.46\,nm$	motor compliance, κ	$0.2\,pN/nm$
cargo - MT distance, h	$15\,nm$	motor rest length, r_0	$40\,nm$
fluorophore radius, r	$3.5\,nm$	motor step size, δ	$8\,nm$
simulation time step, τ	$0.1\,\mu s$	motor stall force, F_s	$7\,pN$
temperature, T	293 K		

S2 Single Molecule Motility Results

Table S2. Single molecule motility results from experiments [2, 3] and simulations of kinesin-1 and kinesin-3 motors. The zero-load microtubule detachment rate, $k_{\text{off},0}$, is calculated by dividing the velocity by the run length.

Motor	**Velocity (nm/s)**		**Run length (nm)**		$\boldsymbol{k_{\text{off},0}}$ $\mathbf{(s^{-1})}$	
	exp	*sim*	*exp*	*sim*	*exp*	*sim*
kin1WT	800 ± 20 [2]	782 ± 13	740 ± 20 [2]	839 ± 61	1.08 ± 0.06	0.93 ± 0.07
kin1Swap	740 ± 10 [3]	735 ± 5	2320 ± 110 [3]	2908 ± 191	0.32 ± 0.02	0.25 ± 0.02
kin3WT	1760 ± 30 [2]	1748 ± 8	7900 ± 200 [2]	7425 ± 518	0.22 ± 0.01	0.24 ± 0.02
kin3Swap	1470 ± 20 [3]	1453 ± 12	3600 ± 170 [3]	3982 ± 284	0.41 ± 0.02	0.37 ± 0.03

S3 Calculation of mean zero-load off rate, $\langle k_{\text{off}} \rangle$

In this section, we will calculate the expectation value of the detachment rate for a Bell's law type detachment process, $\langle k_{\text{off}} \rangle$ when the motor spring is subject to only Brownian fluctuations. According to Bell's law, the detachment is governed by

$$k_{\text{off}} = k_{\text{off},0} \exp(|F|/F_c) \tag{1}$$

where F_c is the critical force of detachment, and $k_{\text{off},0}$ is the zero-load detachment rate.

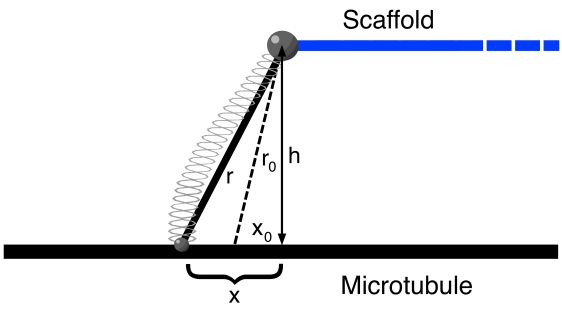

Figure S1. A sketch of a kinesin motor attached to one end of the scaffold.

Let us consider first the case when the spring force exerted by the motor is zero, i.e. the motor extension is within the slack length ($r < r_0$), and the end of the spring can move freely within $|x| < \sqrt{r_0^2 - h^2} \equiv x_0$ (see **Fig. S1**). Here, h is the height of scaffold from the microtubule surface. Within this region, the end point of the spring is uniformly distributed, whereas outside the "slack" length, the probability of finding the end point is Gaussian, namely,

$$P(x) = \begin{cases} A & \text{, for } |x| \le x_0 \\ A \exp\left(-\frac{x^2}{2\sigma_x^2}\right) & \text{, for } |x| > x_0 \end{cases} \tag{2}$$

Normalizing $P(x)$, i.e. integrating from $-\infty$ to $+\infty$, yields

$$A = \frac{1}{\sqrt{2\pi\sigma_x^2} + 2x_0} \ , \tag{3}$$

where σ_x is standard deviation of the end position of the motor spring (motor head). For a simple Hookean spring under the influence of thermal fluctuations, $\sigma_x = \sqrt{k_B T/\kappa_s}$, where κ_s is the compliance of the spring, and $k_B T$ is the thermal energy at a temperature T. While σ_x is also a function of the height h in this case, it is only a weak dependence for small oscillations, and the equation for σ_x given hold for $0.1r_0 < h < 0.75r_0$. Given this position distribution, one can show that the Probability Distribution Function (PDF) of the motor force is given by

$$P(F) = \frac{2(1-P_0)}{\sqrt{2\pi\sigma_F^2}} \exp\left(-F^2/(2\sigma_F^2)\right) \theta(F) + P_0 \delta(F) \ , \tag{4}$$

where σ_F is standard deviation of spring force, $\theta(F)$ is the Heaviside step function, $\delta(F)$ is the Dirac-delta function, and $P_0 \equiv 1/[\sqrt{\pi/2}(\sigma_x/x_0) + 1]$. The factor of two comes from the fact that the force shows up in Eq. (1) as an absolute value, i.e. the spring force F has the same value for x and $-x$. By performing a change of variable, we can find the PDF of k_{off} using

$$P_k(k)dk = P_F(F)\frac{dF}{dk}dk \ . \tag{5}$$

Here, the subscripts k and F have been introduced to distinguish the PDFs written using different variables, and for brevity the subscript "off" has been dropped, i.e. $k \equiv k_{\text{off}}$. Using Eq. (1) one gets

$$P_k(k)dk = P_F\left(F_c \ln\left(\frac{k}{k_0}\right)\right)\frac{F_c}{k}dk \ . \tag{6}$$

We can then calculate the expectation value of the off-rate $\langle k \rangle$ using the following integral

$$\langle k \rangle = \int_{-\infty}^{+\infty} k P_k(k)\, dk = \int_{-\infty}^{+\infty} F_c P_F\left(F_c \ln\left(\frac{k}{k_0}\right)\right) dk \ , \tag{7}$$

and using Eq. (4)

$$\langle k \rangle = F_c \int_{-\infty}^{+\infty} \frac{2(1-P_0)}{\sqrt{2\pi\sigma_F^2}} e^{-\frac{1}{2}\left(\frac{F_c}{\sigma_F}\ln(k/k_0)\right)^2} \theta(F_c \ln(k/k_0)) + P_0 \delta(F_c \ln(k/k_0))\, dk \ . \tag{8}$$

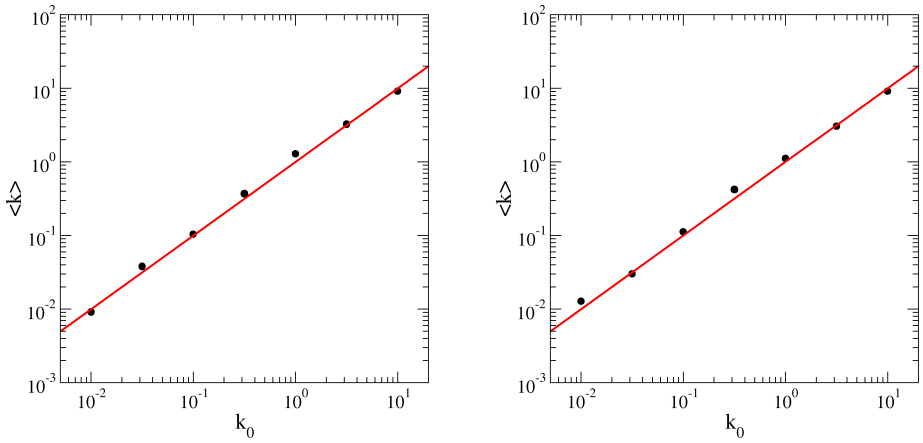

Figure S2. The measured expectation value, $\langle k \rangle$, as a function of zero-load off-rate, k_0. Left panel: kinesin-1, right panel: kinesin-3, Parameters: $r_0 = 40\ nm$, $\kappa_s = 0.2\ pN/nm$, $h = 15\ nm$, and time step $\tau = 0.1\ \mu s$.

By performing the change of variable $y \equiv (F_c/\sigma_F)\ln(k/k_0)$ we will have

$$\langle k \rangle = \frac{2k_0(1-P_0)}{\sqrt{2\pi}} \int_0^{+\infty} e^{\left(-\frac{1}{2}y^2 + \frac{\sigma_F}{F_c}y\right)}\, dy + k_0 P_0 \quad . \tag{9}$$

After completing the exponent to a square, and using $x \equiv (y-\alpha)/\alpha$ with $\alpha \equiv \sigma_F/F_c$ one gets

$$\begin{aligned} \langle k \rangle &= \frac{2k_0\alpha(1-P_0)}{\sqrt{2\pi}} e^{\frac{\alpha^2}{2}} \int_{-1}^{+\infty} e^{-\frac{1}{2}(\alpha x)^2}\, dx + k_0 P_0 & (10)\\ &= k_0(1-P_0)e^{\frac{\alpha^2}{2}}\left(1 + \mathrm{erf}\left(\alpha/\sqrt{2}\right)\right) + k_0 P_0 \\ &\approx k_0(1-P_0)e^{\frac{\alpha^2}{2}}\left[1 + \sqrt{\frac{2}{\pi}}\left(\alpha - \frac{\alpha^3}{6} + \frac{\alpha^5}{40}\right)\right] + k_0 P_0 & (11) \end{aligned}$$

Once again for small oscillations, our earlier approximations hold and $\sigma_F = \sigma_x \kappa_s = \sqrt{\kappa_s k_B T}$. If we further define $\beta \equiv \sigma_F/(\kappa_s x_0)$, one can write $P_0(\beta) \equiv 1/[\beta\sqrt{\pi/2} + 1]$. Combining all of this together yields

$$\langle k \rangle / k_0 \approx (1 - P_0(\beta))e^{\frac{\alpha^2}{2}}\left[1 + \sqrt{\frac{2}{\pi}}\left(\alpha - \frac{\alpha^3}{6} + \frac{\alpha^5}{40}\right)\right] + P_0(\beta) \quad . \tag{12}$$

We performed numerical simulations to determine the average association time of kinesin-1 and -3 motors, and calculated the expectation value $\langle k \rangle$ when only one motor is bound, and it is not stepping. Our results are shown in **Fig. S2** together with the theoretical predictions from Eq. (12) (solid line). While there is not a significant change in the observed off-rate for a relatively force-insensitive motor like kinesin-1 ($F_c = 6.1\ pN$), the correction for motors with lower critical detachment forces can be significant (about a factor of two for kinesin-3, $F_c = 0.5\ pN$). It is also important to note that, despite the assumption of a symmetric off-rate for kinesin-1 in the theoretical calculations, Eq. (12) is in good agreement with numerical measurements.

Finally, in our calculations we assumed that the time step is infinitesimally small, an assumption that is supported by our numerical results. However, for sufficiently large time steps, the upper limit of the integral in Eq. (10) is limited by the time step size since $k_{\max} = 1/\tau$, where τ is time step of simulation. In this case, one can write

$$\langle k \rangle = \frac{2k_0\alpha(1-P_0)}{\sqrt{2\pi}} e^{\frac{\alpha^2}{2}} \int_{-1}^{x_{\max}} e^{-\frac{1}{2}(\alpha x)^2}\, dx + k_0 P_0 \quad , \tag{13}$$

where $x_{\max} = \left(\frac{1}{\alpha}\right)^2 \ln(k_{\max}/k_0) - 1$. For large time steps, this expression can be calculated numerically to obtain a value for the correction.

S4 Sensitivity Analysis

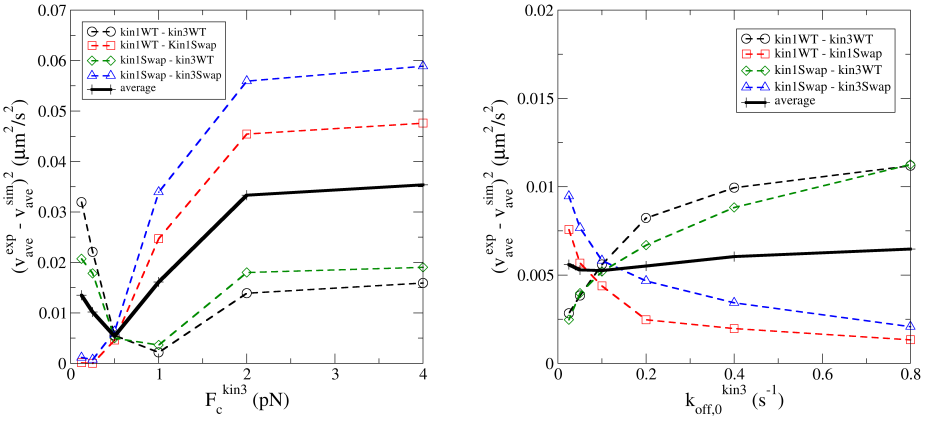

Figure S3. Kinesin-3 parameter sensitivity analysis. To test the sensitivity of the velocity results on the motor parameter choices, we varied F_c and $k_{\text{off},0}$ for kinesin-3 and computed the mean squared error between experimental and simulated velocities. For varying F_c, $k_{\text{off},0}$ was 0.2 s^{-1}, and for varying $k_{\text{off},0}$, F_c was 0.5 pN; k_{reattach} was infinite in both cases. As can be seen, there is a clear minima for $F_c = 0.5\,pN$.

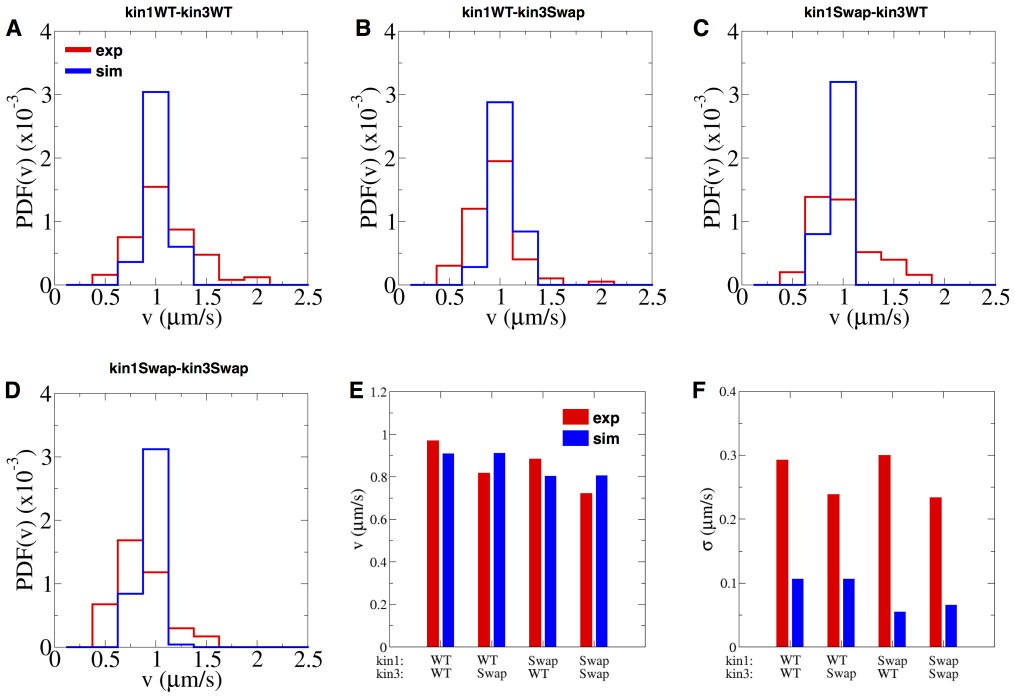

Figure S4. Sensitivity of results to experimentally observed width of velocity distributions. In Fig. 3 of the main text, simulations using an infinite motor on-rate were unable to reproduce the experimental two motor velocity distributions. However, because motors were modeled as stochastic steppers, the standard deviation of velocity, when averaged over N steps is $v_{mean}/\sqrt{N}$, which is 10% for $N = 100$. One possibility is that the two-motor velocity distributions are simply the result of the relatively broad single-motor velocity distributions (e.g. Fig. 1D of the main text). To test this possibility, simulations were repeated using the experimental single-motor velocity distributions for each motor, and the resulting distributions are shown in A-D. A) kin1WT-kin3WT, B) kin1WT-kin3Swap C) kin1Swap-kin3WT, and D) kin1Swap-kin1Swap. E) Mean transport velocities for different motor pairs, comparing experimental (red) to simulated (blue) data. F) Comparison of standard deviation of velocity, σ, for different motor pairs.

S5 Distribution shape optimization

In addition to the mean and standard deviations (Fig. 4A and B of the main text), the similarity of the velocity distributions was also quantified by a modified Chi-squared analysis, namely,

$$\chi^2 \equiv \sum_i \frac{(E_i - S_i)^2}{(E_i + S_i)/2} \quad . \tag{14}$$

Here, for each bin, i, in a given velocity histogram, E_i is the experimental probability and S_i is the simulated probability (e.g. see Fig. 3A-D insets in the main text). The results of the analysis are shown in **Fig. S5** for each of the motor pairs. Comparison of χ^2 values show that the values rose steeply for the two kin1WT combinations for $k_{reattach}$ below 3 s^{-1}, and it increased at higher $k_{reattach}$ for the two pairs containing kin1Swap motors.

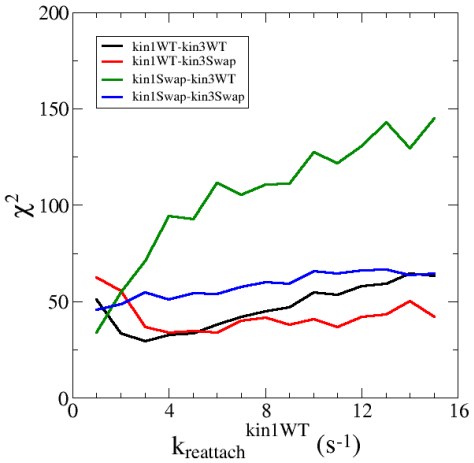

Figure S5. Modified χ^2 error from comparison of experimental and simulation velocity distribution profiles, averaged over 10 data sets.

S6 Motor association times and velocities

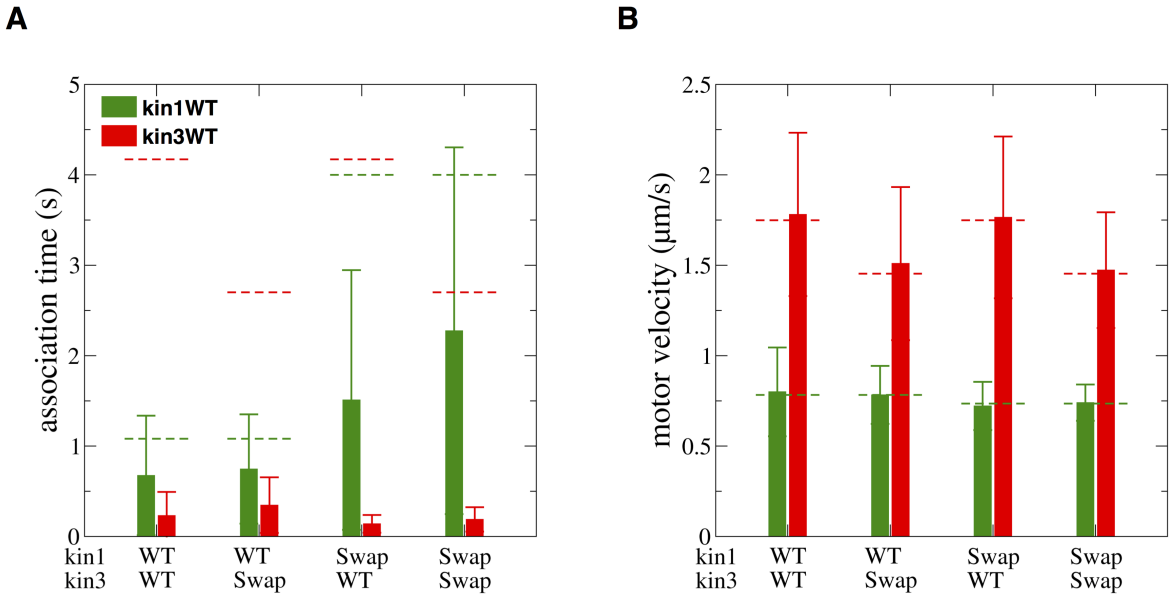

Figure S6. Motor mean association times (A), and velocities (B), for each motor in the complex. Dashed lines show the unloaded values for comparison.

S7 Force traces

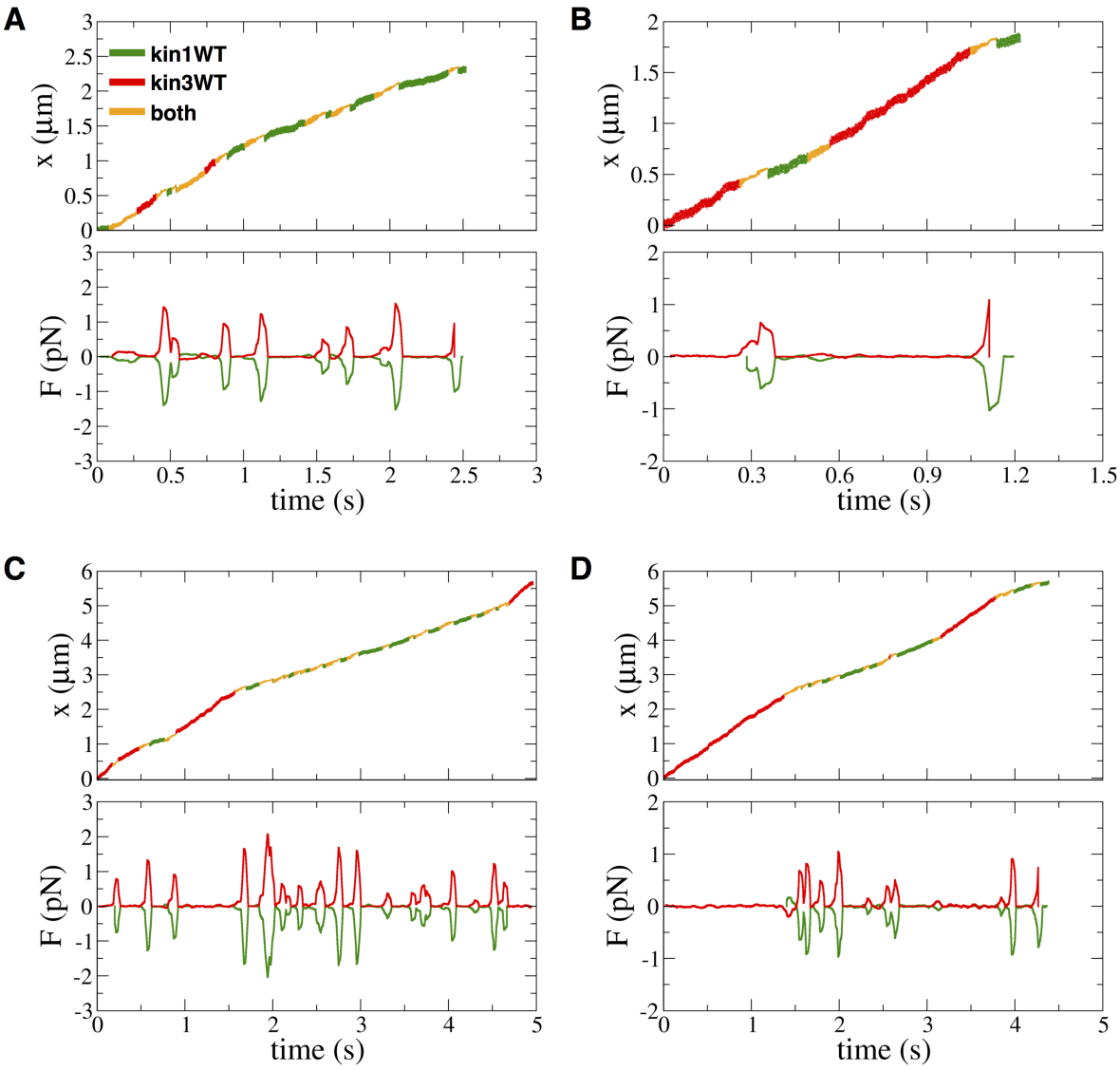

Figure S7. Supplemental instantaneous force trajectories for kin1WT-kin3WT pairs. The force values shown in A-D are averaged using boxcar function where $\langle F_i \rangle = [1/(2M+1)] \sum_{j=-M}^{M} F_{i+j}$ with $M = 250$, and a window size of 50 ms.

Supporting References

[1] Arpağ, G., S. Shastry, W. O. Hancock, and E. Tüzel, 2014. Transport by populations of fast and slow kinesins uncovers novel family-dependent motor characteristics important for in vivo function. *Biophys. J.* 107:1896–1904.

[2] Norris, S. R., V. Soppina, A. S. Dizaji, K. I. Schimert, D. Sept, D. Cai, S. Sivaramakrishnan and K. J. Verhey, 2014. A method for multiprotein assembly in cells reveals independent action of kinesins in complex. *J. Cell Biol.* 207:393–406.

[3] Soppina, V. and K. J. Verhey 2014. The family-specific K-loop influences the microtubule on-rate but not the superprocessivity of kinesin-3 motors. *Mol. Biol. Cell.* 25:2161–2170.

[4] Tomishige, M., D. R. Klopfenstein and R. D. Vale, 2002. Conversion of Unc104/KIF1A kinesin into a processive motor after dimerization. *Science.* 297:2263–2267.